A ferrocene-based carbon–iron lithium fluoride nanocomposite as a stable electrode material in lithium batteries†‡

Raju Prakash,* Ajay Kumar Mishra, Arne Roth, Christian Kübel, Torsten Scherer, Mohammad Ghafari, Horst Hahn and Maximilian Fichtner*

Received 15th September 2009, Accepted 5th December 2009
First published as an Advance Article on the web 15th January 2010
DOI: 10.1039/b919097j

A nanocomposite comprising carbon–iron LiF was prepared by pyrolysis of a mixture of ferrocene and LiF at 700 °C under an argon atmosphere for 2 h. The structure and morphology of the material was characterized by high-resolution transmission electron microscopy (HRTEM), X-ray diffraction (XRD), BET analysis, and Mössbauer spectroscopy. The composite consists of multi-walled carbon nanotubes and onion-type graphite structures in which Fe and Fe_3C nanoparticles are encapsulated, and LiF is dispersed within the carbon matrix. The sample contains both micro- (0.025 $cm^3\ g^{-1}$) and mesopores (0.14 $cm^3\ g^{-1}$), and has a total specific surface area of 82 $m^2\ g^{-1}$. Its charge/discharge performances were studied in the potential range 0.5 V to 4.3 V at a current density of 20.83 mA g^{-1} at 25 °C. It exhibited an initial discharge capacity of 324 mAh g^{-1} with respect to the active mass of FeF_3. After five cycles the capacity reached 280 mAh g^{-1} and is maintained at about 270 mAh g^{-1} over 200 cycles. A reversible specific capacity of about 170 mAh g^{-1} was realized when the potential range was between 1.3 and 4.3 V.

Introduction

The role of lithium batteries in future large-scale energy storage applications, for instance in electrical vehicles, power backups, and other stationary devices, depends primarily on their ability to provide the required key features: high energy density, high power density, rate capability, safety, and extended cyclic stability.[1] Additional factors, such as cost, natural abundance of the inherent materials, and their toxicity, will play an increasingly important role. In this context, iron-based electrochemical storage systems would be of particular interest. Since the performance of a battery depends decisively on the properties of the electrode (cathode and anode) materials, it is necessary to seek and design advanced materials having high reversible storage capacities for lithium.[2] An approach having the potential to attain higher capacities is to utilize several oxidation states of the electrode material by a reversible conversion reaction according to the following equation.[3]

$$M^{n+}X_n + nLi^+ + ne^- \Leftrightarrow nLiX + M$$

Metal fluorides are the most favorable material for the above conversion reaction. Due to the highly ionic nature of their M–F bond, they should theoretically exhibit a much higher output voltage and lithium storage capacity than any other system (*e.g.* TiF_3 767 mAh g^{-1}; VF_3 745 mAh g^{-1}; MnF_3 719 mAh g^{-1}; FeF_3 712 mAh g^{-1}; CoF_3 695 mAh g^{-1}).[4] Until 1970, considerable effort was made to use metal fluorides (AgF_2, NiF_2, CuF_2, CdF_2, HgF_2, CoF_3, BiF_3, *etc.*) as cathode materials for the development of primary lithium batteries, as reviewed in the literature.[5] However, many of the metal fluorides exhibit a limited electrochemical activity with lithium due to their poor electronic conductivity brought about by their large band gap. One of the first reports of metal fluorides as cathode materials for rechargeable Li batteries was published by Seiger *et al.* in 1970,[6a] where the electrochemical studies have shown that the first discharge of NiF_2 could result in over 50% utilization and a limited degree of reversibility. Two decades later, Arai *et al.* reported the electrochemical activity of TiF_3, VF_3, and FeF_3.[6b] These compounds reached a reversible capacity of 80 mAh g^{-1} in the potential range between 4.5 and 2.0 V, which corresponds to the intercalation portion of the M^{3+}/M^{2+} redox couple.[6b] Recently, heterogeneous conversion reactions of TiF_3 and VF_3 at room temperature have been reported.[7] The reversible Li storage capacities of TiF_3 and VF_3 observed were as high as 500–600 mAh g^{-1} between 4.3 and 0.02 V. Later, Badway *et al.* demonstrated that an FeF_3/C nanocomposite, prepared by ball milling, reached an initial discharge capacity of 200 mAh g^{-1} between 4.5 and 2.0 V for the Fe^{3+}/Fe^{2+} redox couple.[8a] A three-electron reduction (Fe^{3+}/Fe^0) was also reported using the same nanocomposite at 70 °C with capacities >500 mAh g^{-1}.[8b] In addition, Wu *et al.* reported that a nanocomposite of FeF_3/MoS_2 or FeF_3/V_2O_5 exhibited better electrochemical performance than undoped FeF_3 electrode in the potential range of 2.0–4.5 V.[9]

Despite intensive efforts, application of metal fluoride cathodes has been largely hampered by partial reaction irreversibility and poor cycling stability.[5–9] Hence, an alternative approach to material synthesis is needed. Encapsulation of transition metal/metal fluoride in carbon might be an effective strategy to improve the cycling performance of batteries. Transition metal oxide

Karlsruhe Institute of Technology (KIT), Institute of Nanotechnology, Postbox 3640, 76021 Karlsruhe, Germany. E-mail: raju.prakash@kit.edu; maximilian.fichtner@kit.edu; Fax: +49-7247-826368

† Electronic supplementary information (ESI) available: Further TEM, EELS, XRD, and electrochemical data. See DOI: 10.1039/b919097j

‡ Dedicated to Professor Rolf W. Saalfrank on the occasion of his 70th birthday.

incorporated carbon electrodes have exhibited better cycling performances in lithium batteries.[10] Recent reports also suggest that iron encapsulated in meso- and macroporous carbon can be used as anodes in Li batteries and reaches a high reversibility and rate performance.[10d] In this respect, encapsulation of metal/metal fluoride in various carbon materials, such as carbon nanotubes (CNTs), carbon fibers, and porous carbon materials, may lead to improved properties.

A number of reports are available in the literature on the formation of nanotubes by chemical vapor deposition (CVD) of organic precursors catalyzed by ferrocene.[11] At temperatures above 500 °C, gaseous ferrocene decomposes spontaneously and completely to form metallic iron according to the following equation as reported in the literature.[12] The iron produced acts as a catalyst for the growth of nanotubes with the carbon atoms from the ferrocene and the other organic precursors. The yield and nature of the nanotubes depend on the preparation method as well as on the precursor used. Use of this method also is of interest for the synthesis of nanowires,[13] nanospheres,[14] and encapsulated metal particles.[15] In all these cases, the multi-step process requires a CVD quartz reactor, expensive carrier gases, and substrates.

$$Fe(C_5H_5)_2 \xrightarrow{>500^\circ C} Fe + H_2 + CH_4 + C_5H_6 + \cdots \text{reactive hydrocarbons}$$

Herein, we show a simple procedure based on the thermal decomposition of a ferrocene/LiF mixture to produce an inexpensive cathode material which exhibits good cyclic stability and reversibility in a fluoride-based Li battery. A nanocomposite is produced, which consists of graphite onions and multi-walled carbon nanotubes which encapsulate the Fe nanoparticles.

Experimental

Sample preparations and processing steps were carried out in an argon-filled glove box and/or using standard Schlenk techniques under an argon atmosphere. Analytical-grade ferrocene and lithium fluoride (Alfa Aesar Co.) were dried at 150 °C under vacuum for 15 h, then ball-milled for 12 h under argon in a planetary ball mill (Fritsch GmbH).

Synthesis

The homogeneous mixture of ferrocene (900 mg, 4.8 mmol) and LiF (375 mg, 14.5 mmol) was placed into a stainless steel reactor (inner diameter, 0.7 cm; length 7 cm) and this was sealed with VCR fittings at both ends inside a glove box. The reactor was placed horizontally inside a tube furnace (GERO) at room temperature. Then, the furnace was heated at a rate of 5 °C min^{-1} to reach the set temperature of 700 °C (in about 2.5 h). After pyrolysis for 2 h, the reactor was cooled to room temperature. Due to various gaseous materials produced during pyrolysis, pressure developed inside the reactor. It was opened carefully inside a glove box in order to release the pressure. The product obtained was a dry, very fine, and soft black powder of >90 wt% of the reactants. The carbon content of the nanocomposite was determined to be 41.5% based on elemental analysis.

Characterization

TEM characterization was performed using an FEI Titan 80–300 operated at 300 kV and a Tecnai F20 STwin operated at 200 kV. Both instruments were equipped with a Gatan imaging filter (Tridiem 863, GIF2001), EDAXs-UTW EDX detectors, and Fischione HAADF-STEM detectors. TEM samples were prepared by dispersion in dry pentane. A droplet was placed onto a carbon grid and allowed to dry for at least 2 h. The grids were sealed and reopened to put them into the TEM, thereby minimizing exposure to the atmosphere to about a minute. The nitrogen physisorption isotherms were measured using a Micromeritics ASAP 2020 system at 77 K. Prior to measurement, the samples were degassed at 350 °C for 12 h. Pore size distributions (PSD) were calculated based on a DFT model[16] assuming slit-shaped pores. The specific surface area was determined according to the BET theory.[17] Powder X-ray diffraction patterns were obtained with a Philips X'PERT diffractometer (Cu-Kα radiation, 2 kW, with X'Celerator RTMS detector, automatic divergence slit). PANalytical X'Pert Data Collector and X'Pert HighScore software were used for data acquisition and evaluation, respectively. The samples to be analyzed were spread onto a silicon single crystal in the glovebox and sealed with an airtight hood made of Kapton foil, which is out of the focus of the spectrometer. The patterns were recorded at 25 °C in a 2θ range between 10 and 80°. The Mössbauer spectra were recorded using a conventional constant acceleration-type spectrometer with a moving source of ^{57}Co in an Rh matrix. The samples to be measured were sealed between kapton foils with a copper support inside a glovebox. The isomer shift was given relative to α-Fe at room temperature. Electrochemical experiments were performed with two electrode-Swagelok-type cells. The positive electrode was fabricated by mixing the nanocomposite and poly(vinyldifluoride-*co*-hexafluoropropylene) (SOLEF 21216/1001) at a weight ratio of 90 : 10. A pure lithium foil (Goodfellow) was used as negative electrode. A layer of glass fiber (GF/D; Whatman) was used as separator. The electrolyte solution was prepared by dissolving 1 M $LiPF_6$ in a mixture (1 : 1 by volume) of ethylene carbonate (EC) and dimethyl carbonate (DMC). Galvanostatic charge–discharge cycling tests were performed using an Arbin BT2000 multi-channel battery testing system at various current densities in the voltage range between 4.3 and 0.5 V. After performing one or several charge–discharge cycles, the electrodes were removed from the cells, washed with anhydrous DMC, and dried under vacuum for 2 h for further analyses.

Results and discussion

The nanocomposite was synthesized by pyrolysis of an intimate ferrocene–LiF mixture in a closed reactor under an argon atmosphere at 700 °C for 2 h. Ferrocene was chosen as a starting material for the synthesis of the nanocomposite, because it is not only an innocuous and inexpensive material, but also can act as both an iron and carbon precursor. The amount of LiF used (approximately 3 mole ratio to Fe) for the synthesis of the nanocomposite was based on the total amount of Fe which can be produced from pyrolysis of the given quantity ferrocene. Energy dispersive X-ray analysis was performed with the nanocomposite and the relative molar ratio of total Fe (Fe/Fe_3C) and

F (from LiF) was observed to be 1 : 2.8. The morphology of the material was examined using transmission electron microscopy (TEM). Fig. 1 shows TEM images of the as-prepared nanocomposite. The overview image reveals iron-rich nanoparticles embedded in a graphitic matrix which contains multi-walled nanotubes and graphitic onions. HAADF-STEM imaging indicates a typical diameter of 2–30 nm for the iron-rich particles, but occasionally particles with up to 100 nm diameter are also observed. The iron-rich particles imaged close to the edge of these aggregates are typically either located inside graphitic nanotubes or embedded inside onion-like graphite spheres. Both iron (α-Fe) and iron carbide (Fe_3C) nanocrystals (identified by their lattice parameters) were detected inside the graphitic onions. Closer inspection of the graphitic matrix revealed a significant number of open-ended tube-like structures as well as inhomogeneities in the onion-like graphitic coating indicating also partial encapsulation of the iron-rich particles by the graphitic matrix (Fig. 1 and Fig. S1, ESI†). HAADF-STEM in combination with local EELS analysis revealed that small amounts of fluorine (presumably as LiF) were present in most of these aggregates (Fig. S2, ESI†). In addition, fairly smooth aggregates exhibiting strong fluorine and noticeable iron signals were present in the material, indicating that these aggregates mainly consist of LiF and iron-rich nanoparticles.

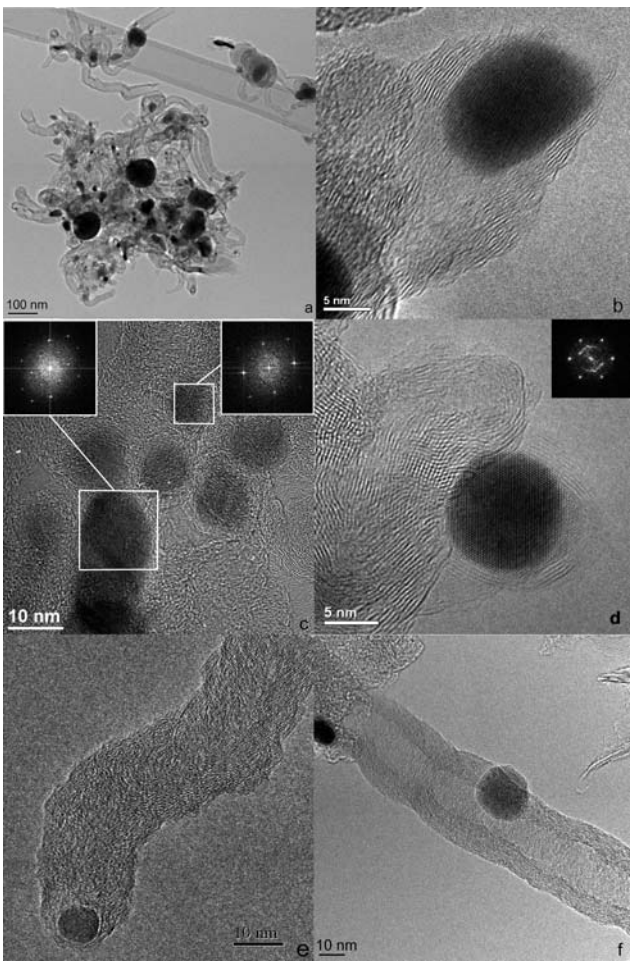

Fig. 1 TEM characterization of the as-prepared carbon–Fe–LiF composites. (a) BF-TEM overview image. (b) An iron-rich nanoparticle in an open tubular graphitic structure. (c) Iron-rich particles confined by onion-like graphitic structures. Based on the observed lattice fringes, the two particles indicated were identified to be α-Fe [001] (top right) and Fe_3C [001] (bottom left). (d) Inhomogeneous graphitic coating of a α-Fe particle imaged in [111] orientation. (e) Iron-rich nano particles inside a tubular graphitic structure. (f) Multi-walled tube-like carbon framework.

The porosity of the material was determined by a nitrogen physisorption measurement at 77 K. The pore size distribution and total pore volume of the composite were calculated according to the DFT model.[16] Fig. 2 displays the adsorption/desorption isotherms, pore size distribution, and pore volume of the composite. The isotherms exhibit a steep increase of the adsorbed gas at very low relative pressures due to the presence of micropores (pore widths below 2 nm) and a pronounced hysteresis loop in the high-pressure range, which is characteristic of materials having mesopores (pore widths between 2 and 50 nm). The sample has a microporous volume of 0.025 $cm^3\ g^{-1}$ and a mesoporous volume of 0.14 $cm^3\ g^{-1}$. According to BET analysis,[17] a total specific surface area of 82 $m^2\ g^{-1}$ is obtained.

To analyze the composition and structure of the composite, powder X-ray diffraction (XRD) experiments were carried out. In Fig. 3, XRD patterns of the ferrocene–LiF mixture before heat treatment and of the nanocomposite formed after pyrolysis are compared. It illustrates that the ferrocene has been converted completely into carbon and iron. The carbon exhibits a pronounced graphite-like diffraction peak corresponding to an average π stacking distance of 3.38 Å. Furthermore, two distinct iron-rich phases (Fe_3C and α-Fe) were identified. The lattice parameters of Fe_3C are: orthorhombic; a = 5.0910 Å, b = 6.7434 Å, c = 4.5260 Å; space group *Pnma* (62), Joint Committee on Powder Diffraction Standards (JCPDS) powder diffraction file (PDF) 035-0772; α-Fe, cubic $a = b = c$ = 2.8664 Å; space group *Im3m* (229), PDF 006-0696. The formation of Fe_3C had been expected due to the dissolution of carbon atoms in Fe during nanotube growth at high temperature.[15] No obvious reflections corresponding to iron oxides or iron fluorides are found in the XRD patterns, which indicates that the metallic iron nanoparticles have neither oxidized nor reacted with LiF during

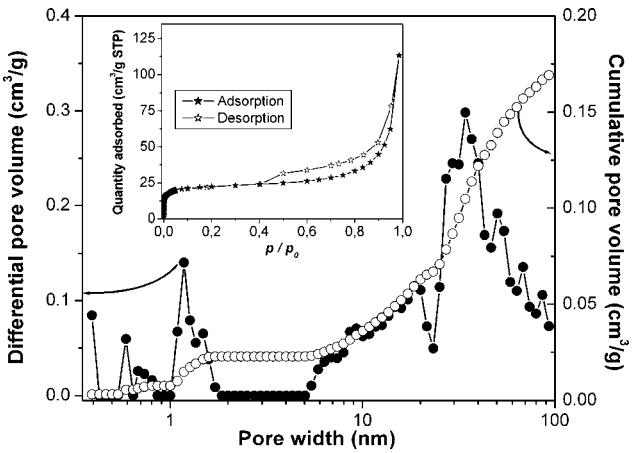

Fig. 2 Cumulative pore volume and differential pore volume as a function of pore width of the nanocomposite measured at 77 K. Inset: N_2 isotherm.

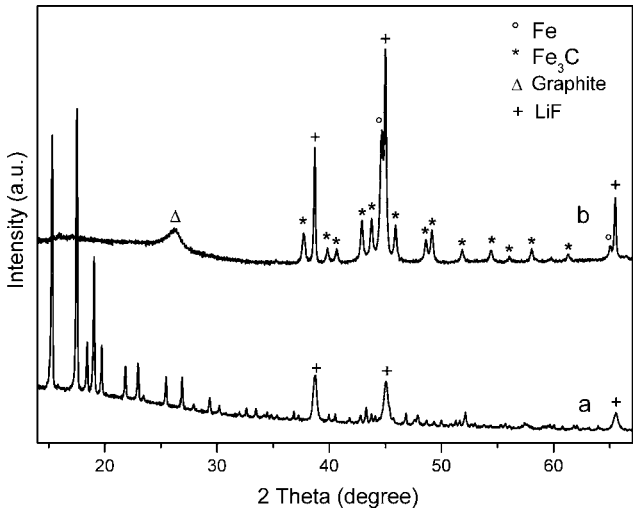

Fig. 3 XRD patterns of (a) a ball-milled mixture of ferrocene (unassigned peaks; PDF:00-029-1711) and LiF (PDF: 00-004-0857) and (b) the nanocomposite formed after pyrolysis of the mixture at 700 °C for 2 h under an argon atmosphere.

pyrolysis. Mössbauer spectroscopic data corroborate the XRD data. The Mössbauer spectrum of the composite recorded at 300 K consists of two well-resolved spectra with magnetic hyperfine fields, B_{hf}^1 and B_{hf}^2 (Fig. 4). The first Zeeman sextet ($B_{hf}^1 = 33.2$ T; isomer shift $\delta = 0$ mm s^{-1}) is in good agreement with the Mössbauer parameters observed for α-Fe with a BCC structure at 300 K. The second ferromagnetic component with an average hyperfine magnetic field $<B_{hf}^2>$ of 20.6 T and an isomer shift of $\delta = 0.179$ mm s^{-1} can be attributed to the iron content in the Fe_3C with a cementite structure.[18] The relative areas of the ferromagnetic Fe and Fe_3C were estimated to be 54% and 46%, respectively.

Galvanostatic charge/discharge experiments were performed at different potential ranges at room temperature to evaluate electrochemical properties of the nanocomposite (Fig. 5). The voltage profiles of the nanocomposite used as a positive electrode in Li cells are shown in Fig. 5a (inset). The charge/discharge specific capacities are determined based on the mass of the active

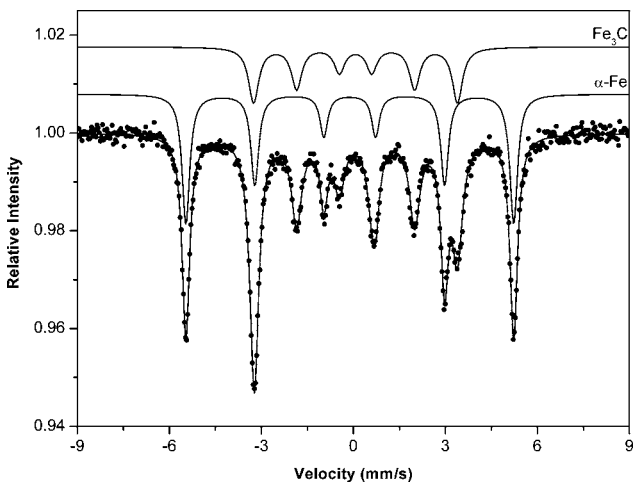

Fig. 4 Mössbauer spectrum of the nanocomposite at 300 K. The solid lines are the least square fit to the experimental data in the dotted lines.

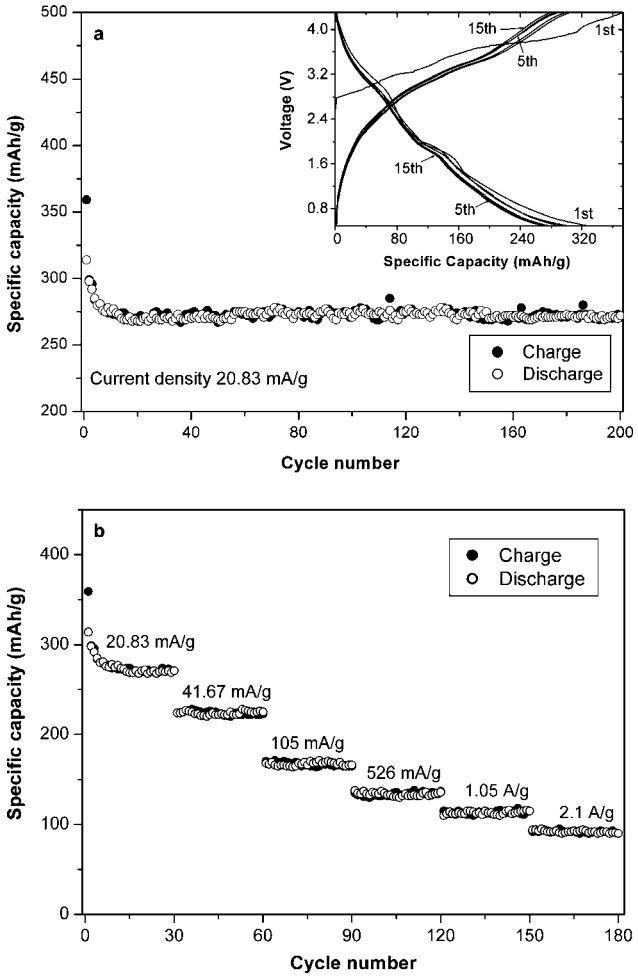

Fig. 5 Electrochemical characterization of the carbon–Fe–LiF nanocomposite. (a) Specific capacity as a function of cycle number. Inset: Galvanostatic charge/discharge time *vs.* voltage. (b) Specific capacity *vs.* cycle number at various current densities; the nanocomposite cycled between 4.3 and 0.5 V for 30 cycles at each current density.

material FeF_3 (calculated from the amount of LiF and Fe present in the composite electrode). In the potential range between 4.3 and 0.5 V, it exhibits three plateaus in the discharging processes. The given voltage profiles are consistent with that of metal fluoride systems that have already been reported in literature.[6–8] However, the observed short-flat plateaus indicated that the active material is not converted completely. At an applied current density of 20.83 mA g^{-1}, the first charge and discharge capacities are as high as 372 and 324 mAh g^{-1}, respectively. The first plateau during discharge between 3.5 and 2.5 V with a capacity of about 80 mAh g^{-1}corresponds to the Fe^{3+}/Fe^{2+} redox couple in the lithium insertion region. The second plateau between 2.5–1.3 V with a capacity of about 120 mAh g^{-1} corresponds to the conversion reaction. The third sloped region between 1.3–0.5 V yielded a capacity of about 120 mAh g^{-1} and can be due to the carbon component or an interfacial interaction of lithium within the M/LiX matrix as proposed in literature.[3,5,6] When the charge/discharge reactions were performed between 4.3 and 1.3 V at 20.83 mA g^{-1}, it delivered an initial discharge capacity of 190 mAh g^{-1} for the Fe^{3+}/Fe^0 redox couple. After 5

cycles, the capacity remained stable at about 170 mAh g^{-1} (see Fig. S3, ESI†), and the capacity retention ratio was 90% after 30 cycles.

The specific capacity is shown as a function of the cycle number in Fig. 5a. It is obvious that the capacity decreases over the first five cycles and then stabilizes at 280 mAh g^{-1}, which is maintained at 275 mAh g^{-1} even after 200 cycles. The loss of capacity between 5 and 200 cycles was found to be less than 3%. The coulombic efficiency (calculated from the ratio of discharge capacity to charge capacity) in the first cycle is 86%. After this, the value is always in the range between 97 and 100%.

Additionally, the nanocomposite electrode exhibits a good rate capability due to improved diffusion kinetics. At first, the cell was cycled at 20.83 mA g^{-1} for 30 cycles, and then the current densities were increased in a stepwise manner to 2.1 A g^{-1} every 30 charge/discharge cycles (Fig. 5b). It is obvious from the figure that the reversible capacities decrease as the current densities increase, *e.g.* at 0.10 and 1.05 A g^{-1}, the reversible capacities reach 175 and 120 mAh g^{-1}, respectively. However, it is interesting that the capacity remains stable over the entire 30 cycles at a given current density. If the current density is lowered again to 20.83 mA g^{-1} after 180 cycles, a capacity of 260 mAh g^{-1} can still be attained.

In order to confirm the formation of FeF_3 by a three-electron reaction of LiF and Fe, TEM, SAED and *ex situ* XRD analyses were performed using the nanocomposite electrode which was charged to 4.3 V at the current density of 20.83 mA g^{-1}. Fig. 6 shows TEM and SAED images of the nanocomposite electrode at the charged state. The TEM images exhibit iron-rich aggregates of particles embedded in graphite onions as part of larger graphitic aggregates and FeF_3 nanoparticles (for local EELS/EDX analysis, see Fig. S4, ESI†). The SAED patterns of the FeF_3 aggregates reveal well-defined diffraction rings corresponding to *d*-spacings of 3.73, 2.67, 2.24, 1.86, and 1.68 Å, which allow for a clear identification as FeF_3 (trigonal, $a = b = 5.2000$ Å, $c = 13.3230$ Å; space group $R\bar{3}c$ (167), PDF 033-0647). In addition, it exhibits a weak diffraction ring corresponding to a *d*-value of 3.32 Å, which is in agreement with the main Bragg peak (110) of FeF_2 (tetragonal, $a = b = 4.7035$ Å, $c = 3.3056$ Å; space group *P42/mnm* (136), PDF 045-1062).

The XRD pattern of the composite electrode exhibits a distinct Bragg peak (012) of FeF_3 at 23.83° (PDF 033-0647). Consequently, the Fe signals vanish completely, while the Fe_3C and LiF peak intensities decrease (see Fig. S5, ESI†). It suggests that metallic iron reacts readily with LiF to form FeF_3. On the other hand, reactivity of the orthorhombic Fe_3C towards lithium fluoride is much less than those of metallic iron (cubic). This may be one of the reasons that the specific capacity is lower than the theoretical value. The XRD pattern of the nanocomposite electrode recorded at the end of the first cycle (*i.e.* discharged state) shows a similar pattern to that of the nanocomposite. XRD patterns of the electrode material after the 50th charged and 50th discharged states are shown in Fig. 7. The XRD data of the charged state of the electrode reveals that FeF_3 remained as the only significant phase developed. However, a small quantity of FeF_2 is formed during cycling as observed by a Bragg reflection (110) at 26.8° (PDF 045-1062). In the discharged state, both FeF_3 and FeF_2 peaks disappeared and metallic Fe phase developed. These results illustrate the reversible behavior of the nanocomposite electrode material. But, at the moment it is not clear whether the FeF_3 and FeF_2 are converting back only to Fe phase or both Fe and Fe_3C phases.

To study the cyclic stability of the material, at first the original nanocomposite was ball-milled for 6 h and then charge/discharge experiments were performed between 4.3 and 0.5 V using the electrode made of the ball-milled sample at a current density of 20.83 mA g^{-1}. First charge and discharge capacities of 488 and 392 mAh g^{-1}, respectively, were obtained. Despite the higher initial capacities, the ball-milled material exhibits a rapid loss of capacity with cycling. After 50 cycles, the charge and discharge

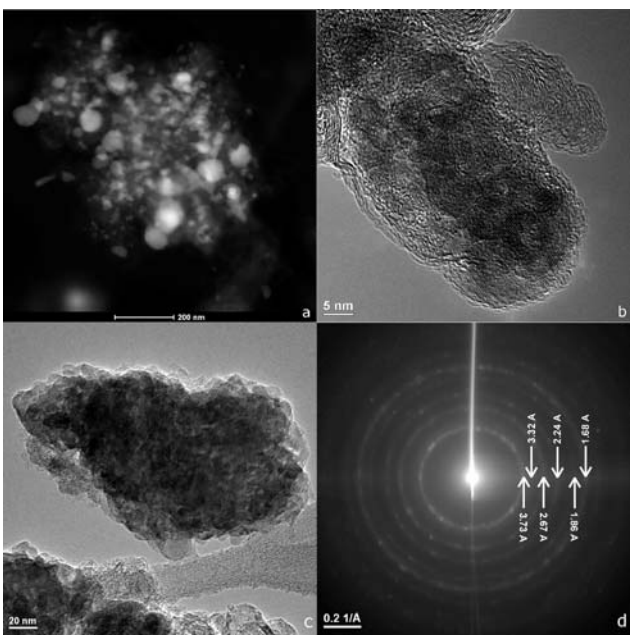

Fig. 6 TEM characterization the nanocomposite electrode after the 1st charging experiment: (a) HAADF-STEM overview image. (b) HRTEM image showing iron-rich nanoparticles embedded in a graphite matrix. (c) Overview image of a FeF_3 aggregate. (d) Electron diffraction pattern of such an aggregate dominated by diffraction rings of FeF_3 and a weak FeF_2 signal.

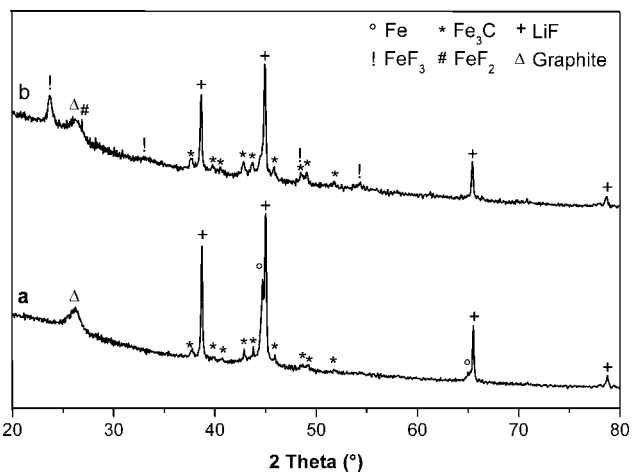

Fig. 7 XRD patterns of the nanocomposite electrode after performing charge/discharge cycles between 4.3 and 0.5 V at a current density of 20.83 mA g^{-1} for 50 cycles. (a) Discharged state. (b) Charged state.

capacities were reduced to 90 and 87 mAh g^{-1}, respectively. The most likely reason for the cyclic instability in this case is the destruction of the graphitic nano-encapsulation by ball milling, which in turn leads to the disintegration of the materials during phase transformation resulting in an electrical disconnection of the particles. In contrast, the original nanocomposite under identical conditions shows excellent cyclic stability, which presumably comes from the carbon framework that may play a role in integrating the active materials. However, the composite exhibits a moderate capacity. Only about 40% of the theoretical value of FeF_3 (712 mAh g^{-1}) was achieved. Hence, more work is needed to optimize its capacity, such as, reduction/removal of Fe_3C, produce uniform particle size/distribution, reduce the carbon content, obtain more Fe-encapsulated carbon nanotubes, *etc.* Therefore, efforts are currently being undertaken to optimize the nanocomposite, with respect to carbon, iron and fluoride contents as well as their ratios.

Conclusions

We report a facile method of synthesis of a carbon-encapsulated Fe–LiF nanocomposite starting from a ferrocene and LiF mixture. The nanocomposite consists of multi-walled carbon nanotubes and onion-type graphite structures in which iron particles are encapsulated, and LiF is dispersed throughout the matrix. The nanocomposite employed as the cathode of a Li battery exhibited a reversible capacity of 280 mAh g^{-1} in the potential range 0.5–4.3 V and of 170 mAh g^{-1} in the range of 1.3–4.3 V at a current density of 20.83 mA g^{-1}. The nanocomposite cathode showed capacity retention of 83.5% after 200 cycles, as well as a durable rate capability. However, efforts are in progress to optimize the Fe and carbon contents of the nanocomposite in order to increase the capacity of the system. In any case, it is believed that this synthetic method opens a way for the preparation of different kinds of inexpensive carbon-encapsulated nanocomposites. Future work will also focus on the mechanistic understanding of the system.

Acknowledgements

Financial support by the MWK project "*e-drive*" (State of Baden-Württemberg) and "*Verbund Süd*"is gratefully acknowledged. The author RP thanks Dr Frank Hennrich for fruitful discussions.

References

1 (*a*) A. Patil, V. Patil, D. W. Shin, J.-W. Choi, D.-S. Paik and S.-J. Yoon, *Mater. Res. Bull.*, 2008, **43**, 1913; (*b*) M. S. Whittingham, *Chem. Rev.*, 2004, **104**, 4271; (*c*) M. Winter and R. J. Brodd, *Chem. Rev.*, 2004, **104**, 4245.
2 (*a*) Y.-G. Guo, J.-S. Hu and L.-J. Wan, *Adv. Mater.*, 2008, **20**, 2878; (*b*) J. M. Tarascon and M. Armand, *Nature*, 2001, **414**, 359; (*c*) T. J. Patey, A. Hintennach, F. La Mantia and P. Novák, *J. Power Sources*, 2009, **189**, 590; (*d*) E. Frackowiak, K. Kierzek, G. Lota and J. Machnikowski, *J. Phys. Chem. Solids*, 2008, **69**, 1179.
3 (*a*) P. Poizot, S. Laruelle, S. Grugeon, L. Dupont and J. M. Tarascon, *Nature*, 2000, **407**, 496; (*b*) S. Laruelle, S. Grugeon, P. Poizot, M. Dolle, L. Dupont and J.-M. Tarascon, *J. Electrochem. Soc.*, 2002, **149**, A627.
4 H. Li, P. Balaya and J. Maier, *J. Electrochem. Soc.*, 2004, **151**, A1878.
5 (*a*) K. M. Abharam, *J. Power Sources*, 1981, **7**, 1; (*b*) G. G. Amatucci and N. Pereira, *J. Fluorine Chem.*, 2007, **128**, 243.
6 (*a*) H. N. Seiger, A. E. Lyall, R. C. Shair, in *Proceedings of the 6th International Symposium on Power Sources 2: Res: Develop. Non-Mech. Elec. Power Sources*, 1970, p.267; (*b*) H. Arai, S. Okada, Y. Sakurai and J. Yamaki, *J. Power Sources*, 1997, **68**, 716.
7 H. Li, G. Richter and J. Maier, *Adv. Mater.*, 2003, **15**, 736.
8 (*a*) F. Badway, N. Pereira, F. Cosandey and G. G. Amatucci, *J. Electrochem. Soc.*, 2003, **150**, A1209; (*b*) F. Badway, F. Cosandey, N. Pereira and G. G. Amatucci, *J. Electrochem. Soc.*, 2003, **150**, A1318; (*c*) M. Nishijima, I. D. Gocheva, S. Okada, T. Doi, J.-i. Yamaki and T. Nishida, *J. Power Sources*, 2009, **190**, 558.
9 (*a*) W. Wu, X. Wang, X. Wang, S. Yang, X. Liu and Q. Chen, *Mater. Lett.*, 2009, **63**, 1788; (*b*) W. Wu, Y. Wang, X. Wang, Q. Chen, X. Wang, S. Yang, X. Liu, J. Gao and Z. Yang, *J. Alloys Compd.*, 2009, **486**, 93.
10 (*a*) A. Concheso, R. Santamaría, R. Menéndez, J. M. Jiménez-Mateos, R. Alcántara, P. Lavela and J. L. Tirado, *Carbon*, 2006, **44**, 1762; (*b*) Y. NuLi, P. Zhang, Z. Guo and H. Liu, *J. Electrochem. Soc.*, 2008, **155**, A196; (*c*) W.-L. Yao, J.-L. Wang, J. Yang and G.-D. Du, *J. Power Sources*, 2008, **176**, 369; (*d*) Y.-S. Hu, P. Adelhelm, B. M. Smarsly, S. Hore, M. Antonietti and J. Maier, *Adv. Funct. Mater.*, 2007, **17**, 1873.
11 (*a*) O. Zhou, H. Shimoda, B. Gao, S. Oh, L. Fleming and G. Yue, *Acc. Chem. Res.*, 2002, **35**, 1045; (*b*) O. Similjanic, B. L. Stansfield, J.-P. Dodelet, A. Serventi and S. Desilets, *Chem. Phys. Lett.*, 2002, **356**, 189; (*c*) K. Hata, D. N. Futaba, K. Mizuno, T. Namai, M. Yumura and S. Iijima, *Science*, 2004, **306**, 1362; (*d*) F. Lupo, J. A. Rodriguez-Manzo, A. Zamudio, A. L. Elias, Y. A. Kim, T. Hayashi, M. Muramatsu, R. Kamalakaran, H. Terrones, M. Endo, M. Rühle and M. Terrones, *Chem. Phys. Lett.*, 2005, **410**, 384; (*e*) A. Barreiro, S. Hampel, M. H. Rümmeli, C. Kramberger, A. Grüneis, K. Biedermann, A. Leonhardt, T. Gemming, B. Büchner, A. Bachtold and T. Pichler, *J. Phys. Chem. B*, 2006, **110**, 20973; (*f*) Nasibulin, S. D. Shandakov, A. S. Anisimov, D. Gonzalez, H. Jiang, M. Pudas, P. Queipo and E. I. Kauppinen, *J. Phys. Chem.*, 2008, **112**, 5762.
12 A. Leonhardt, S. Hampel, C. Mueller, I. Moench, R. Koseva, M. Ritschel, D. Elefant, K. Biedermann and B. Buechnet, *Chem. Vap. Deposition*, 2006, **12**, 380.
13 (*a*) L. Pan, M. Zhang and Y. Nakayama, *J. Appl. Phys.*, 2002, **40**, 2791; (*b*) H. M. Cheng, F. Li, X. Sun, S. D. M. Brown, M. A. Pimenta, A. Marucci, G. Dresselhaus and M. S. Dresselhaus, *Chem. Phys. Lett.*, 1998, **289**, 602.
14 (*a*) N. Sano, H. Akazawa, T. Kikuchi and T. Kanki, *Carbon*, 2003, **41**, 2159; (*b*) X. Liu, B. Huang and N. J. Coville, *Carbon*, 2002, **40**, 2791.
15 (*a*) H. Song and X. Chen, *Chem. Phys. Lett.*, 2003, **374**, 400; (*b*) M. Yudasaka, R. Kikuchi, Graphitization of Carboneous Materials by Ni, Co and Fe, in *Supercarbon Synthesis, Properties and Applications*, ed. S. Yoshimura, R. P. H. Chang, Springer, Berlin, 1998, pp. 99–105.
16 P. A. Webb and C. Orr, *Analytical Methods in Fine Particle Technology*, Micromeritics Instrument Corporation, Norcross, 1st edn, 1997.
17 S. Brunauer, P. H. Emmett and E. Teller, *J. Am. Chem. Soc.*, 1938, **60**, 309.
18 (*a*) T. Shinjo, F. Itoh, H. Takaki, Y. Nakamura and N. Shikazono, *J. Phys. Soc. Jpn.*, 1964, **19**, 1252; (*b*) M. Ron, H. Shechter, A. A. Hirsch and S. Niedzwiedz, *Phys. Lett.*, 1966, **20**, 481.

